AN ABSTRACT OF THE THESIS OF

Elizabeth Helen McHugh for the degree of Master of Science in Ocean, Earth and Atmospheric Sciences presented on September 30, 2013

Title: The Leading Edge of a Tropical Instability Wave: Interpretation as a Gravity Current

Abstract approved:

_____

James N. Moum

A sharp temperature front, oriented along the south-west corner of the leading edge of a Tropical Instability Wave (TIW) warm trough, was encountered at 0°N, 140°W on November 2, 2008 and detected by a 0.45°C increase in SST that occurred over 7 s. The distinct SST signal was observed at three different locations within a 5 km radius. The abrupt change in SST was accompanied by a 0.26 psu drop in sea surface salinity and a 0.5 m s^{-1} increase in the near surface zonal velocity. The front was oriented west-northwest and propagated at a speed of 0.56 ± 0.01 m s^{-1}. Sub-surface adjustments that coincided with the passage of the front reached nearly 70 m deep and increased both stratification and vertical shear above the Equatorial Undercurrent. The warm side of the front was

composed of a turbulent, 40 m thick, buoyant fluid that overtook south-southwestward flowing equatorial cold-tongue water, forcing the denser water to be subducted below and accelerated along its previous trajectory. The lower 40% of the buoyant flow was composed of a mixture of fluids from both sides of the front. These observations indicate that the buoyant fluid behind the front was driven by the hydrostatic pressure gradient across the front and flowed as a gravity current. Comparisons with two-dimensional, analytical, gravity current models suggest that the buoyant current was in a state of decay at the time it was observed, and the propagation speed of the temperature front was not fully accounted for by the driving forces of the gravity current at its leading edge. It is hypothesized that large scale dynamics associated with the TIW sharpened the hydro-static pressure gradient across the front to an extent that allowed for the generation of a buoyant gravity current to propagate ahead of the mesoscale wave, after which vertical mixing between the buoyant current and the subducted ambient fluid became responsible for the decay of the current's internal driving forces.

The Leading Edge of a Tropical Instability Wave: Interpretation as a Gravity Current

by

Elizabeth Helen McHugh

A THESIS

submitted to

Oregon State University

in partial fulfillment of

the requirements for the

degree of

Master of Science

Presented September 30, 2013

Commencement June 2014

Master of Science thesis of Elizabeth Helen McHugh presented on September 30 2013.

APPROVED:

_____

Major Professor, representing Ocean, Earth and Atmospheric Sciences

_____

Dean of the College of Earth, Ocean and Atmospheric Sciences

_____

Dean of the Graduate School

I understand that my thesis will become part of the permanent collection of Oregon State University libraries. My signature below authorizes release of my thesis to any reader upon request.

_____

Elizabeth Helen McHugh, Author

ACKNOWLEDGMENTS

Jim Moum, The Ocean Mixing Group, and R.-C Lien acquired the data used within. Alexander Perlin and the Ocean Mixing Group provided processing algorithms used to refine data. Algorithm to compute front speed from equation 1) provided by Martine Hoecker-Martinez. Jim Moum, Bill Smyth, Simon de Szoeke, Emily Shroyer and Sally Warner provided edits and suggestions for the manuscript.

TABLE OF CONTENTS

LIST OF FIGURES

LIST OF TABLES

1. Introduction

The general circulation along the equator in the Pacific can be described by the easterly Trade winds that blow along the equator, the westward flowing South Equatorial Current (SEC) between 2°S and 3°N, and the underlying, subsurface, eastward return flow of the Equatorial Undercurrent (EUC). Equatorial divergence occurs in response to poleward Ekman transport by the Trade winds, and results in the upwelling of cold water along the equator. During Boreal summer, increased solar heating warms the northern tropical Pacific and draws the Inter-Tropical Convergence Zone (ITCZ) north of the equator. The ITCZ enhances precipitation, thus freshening and stabilizing the warm pool below. South easterly trade winds extend beyond the equator to the northward shifted ITCZ, increasing evaporation over the equator and inducing coastal upwelling along the eastern boundary (de Szoeke et al. 2007). Both upwelling and evaporation cool the mixed layer and contribute to the formation of a cold tongue, which extends westward along the equator from the coasts of Ecuador and Peru. The juxtaposition of the cold tongue with the warm fresh pool to its north, and to a mildly warm pool relative to the cold tongue in the south, results in equatorial fronts in both hemispheres that span zonally the length of the cold tongue.

To the north of the SEC lies the North Equatorial Counter Current (NECC), a broad, intermittent, eastward flowing current that usually extends from

5°N to 10°N. The shear generated between the aforementioned zonal jets, coupled with equatorial temperature fronts, become unstable during boreal summer and fall, resulting in westward propagating planetary waves (Philander 1976, 1978; Qiao and Weisberg 1998, Cox 1980). Tropical Instability Waves (TIW), as these are often called, drive meridional perturbations of the equatorial zonal jets and fronts within their path, causing them to meander about the equator (Legeckis 1977; Lyman et al. 2007). The perturbed fronts are oriented into poleward pointing cusps (Fig. 1), which are observed in satellite images of Sea Surface Temperature (SST) propagating westward (Legeckis 1977; Chelton et al. 2000). Between cold cusps, trains of anti-cyclonic, coherent, vortices can form between the SEC and the NECC (Qiao and Weisberg 1995; Kennan and Flament 2000; Holmes et al. 2013).

The Equatorial Internal Wave Experiment (EQUIX) was a collaborative effort designed to study previously unresolved microstructure below the equatorial cold tongue at 0°N, 140°W. During a 16-day Intensive Observation Period (IOP), the trailing (eastern) edge of a TIW cold cusp translated southward through the EQUIX site. The intent of this thesis is to provide a detailed description of the front by (1) documenting the observations surrounding the front, (2) establishing the local speed and orientation of the front, (3) geographically relating local, small-scale features of the front to the mesoscale features associated with the TIW and (4) describing the local, non-linear

dynamics of the front as a gravity current driven by the hydrostatic pressure gradient across the front, independent of the TIW.

The variability associated with TIWs varies with latitude and is composed of two distinct waves with different periods, but with near identical zonal wavelength (Lyman et al. 2007). Within a degree of the equator, TIW-associated variability is strongest in meridional velocity. The equatorial meridional velocity variability occurs over a 17-day period, is most intense at 140°W and correlates to the sub-surface temperature variability at 2°N and 2°S at 140°W. Away from the equator at 5°N, variability is greatest in sub-surface temperature, independent of longitude, and oscillates over a 33-day period. TIW-related variability within a degree of the equator is suspected to be independent of the variability further north, and propagates at nearly twice the rate (Flament et al. 1996; Kennan and Flament 2000; Lee et al. 2012).

Instances of detailed in-situ measurements across the North Equatorial Front during the TIW season are limited. Previous observations have been made between 2°N and 4°N along 140°W (Johnson 1996; Kennan and Flament 2000) and at the equator (Lien et al. 2008), but not at 0°N, 140°W. Johnson (1996) observed the leading (western) edge of a westward propagating cold water cusp. There, southward flowing warm, fresh water and northward flowing cold-cusp water collided at ~2°N and resulted in the subduction of the denser cold-cusp water. Locally, the front was not in geostrophic balance and the dynamics of the

convergence and subduction were better described by a balance between nonlinear advection and pressure gradient forces. Observations agreed well with solutions obtained through the Benjamin (1968) dissipative lock-exchange model.

North of the equator at 125°W, the far southern portion of the leading (trailing) edge of a TIW warm trough (cold-cusp) was encountered by a Lagrangian float (Lien et al. 2008). The kinematics of the front were not fully resolved; however, the amplitude of turbulent mixing at the front was compared to mixing at varying phases of the sub-surface variability of the TIW. Here, the front signified the transitional phase from cold to warm temperatures. It was determined that turbulence was stronger below the front, than during any other phase of the wave.

Vertical mixing along the equator is important because it cools the surface mixed layer, which affects the global head budget, and it supplies nutrients to the photic zone, which increases primary productivity and affects the global CO2 budget. The turbulent vertical mixing at the base of the shear layer was found to be enhanced in the presence of TIWs (Moum et al. 2009). TIWs are complicated and highly non-linear. The westward traveling perturbations of the north equatorial SST front are often used to define the horizontal structure of TIWs in satellite images. These images are capable of confirming the presence of TIWs, but are not able to resolve the small scale structure of these fronts which provide

clues about the three-dimensionality and non-linear dynamics associated with these ubiquitous waves.

Methods are described in section 2. Observations made during the IOP are described in section 3, with a focus on mesoscale observations of the TIW from satellite images in 3a, a summary of the in-situ observations obtained through the EQUIX array in 3b, and a detailed description of the front in 3c. Section 4 focuses on the kinematics of the front, beginning with a calculation to determine the propagation speed and orientation of the front in 4a, a brief summary of the observations from the perspective of a reference frame moving with the front in 4b, an investigation into the two-dimensionality of flow above the EUC in 4c, and finally a description of the vertical structure of the front in 4d. Estimates for the front speed, based on analytical, inviscid 2-dimensional gravity current models, are explicitly computed in section 5, followed by a discussion of the validity of these models and the relevance of their results to dynamics of the front in section 6, and a brief conclusion in section 7.

2. Methods

a. EQUIX Array

An Intensive Observational Period (IOP) of EQUIX was composed of shipboard microstructure profiling off the Research Vessel (RV) Wecoma in addition to the EQUIX upper surface buoy (provided by The University of Washington's (UW) Applied Physics Laboratory (APL) and the National Oceanic Atmospheric Association's (NOAA) Tropical Atmosphere-Ocean (TAO) mooring fitted with additional equipment. Inoue et al. (2012) provides a complete and detailed account of instruments used, sampling frequency and spatial and vertical resolution.

The RV Wecoma's Data Acquisition System (DAS) provides meteorological data including SST and surface salinity at 0.5 Hz and a hull mounted 300-kHz ADCP that resolved the upper 10 m to 120 m. The Chameleon profiler provided by the Oregon State University Ocean Mixing Group, measured pressure, conductivity, temperature, optical backscatter and shears with continuous vertical resolution between 10 m and 200 m approximately every 7 min.

The EQUIX mooring was fitted with a 300 kHz ADCP at 90 meters, and 20 Seabird SB37 CTD sensors sampling temperature and salinity every 7 s. One

SB37 was mounted at the surface and the other 19 were mounted between 20 m and 50 m.

The TAO array mooring at 0°N, 140°W provided SST sampled every 10 minutes. A χ-pod was mounted at 18 m depth during EQUIX and samples temperature at 10 Hz.

b. Satellite Data

Satellite images of SST are used in conjunction with data obtained by the EQUIX array. SST data is obtained from both the Moderate Resolution Imaging Spectroradiometer (MODIS) Aqua and Terra Satellites, and NASA's Tropical Rainfall Measuring Mission's (TRMM) Microwave Imager (TMI). MODIS Aqua and Terra SST data, processed by NASA's Physical Oceanography Distributed Active Archive Center (PO.DAAC), provides 4 km resolution and is available in both daily and 8-day composite averages. TRMM TMI SST data is available at 1/4° resolution and 3-day composite averages.

3. Observations

a. Satellite observations

Fig. 1 shows successive images of adjacent three day composite averages of Tropical Rainfall Measuring Mission (TRMM) Microwave Imager (TMI) SST. The cold tongue, extends close to 145°W over the first three days of the IOP (Fig 1a). Over the next 18 days, it meanders its way westward to nearly 150°W with the active TIW.

The North Equatorial Front, here defined as the interface along the 25 °C isotherm, is displaced by the TIW, with peaks extending close to 4°N and troughs coming close to and sometimes traversing the equator. Similar patterns are also present in the Southern Hemisphere (not shown). The peaks propagate westward with the TIW at a rate of $\sim$0.4 m s^{-1}. Circular pools of relatively cool water can be seen as yellow patches northeast of cold cusp peaks, centered around 5°N, which suggest mixing of temperature by the anti-cyclonic eddy circulation and the possible existence of vortices at their centers.

Vectors representing the daily-averaged near-surface velocities from the hull mounted 300-kHz ADCP on the RV Wecoma are plotted in Fig. 1. Near surface velocities of ~1 m s^{-1} point NNE on October 24 (blue vector, Fig. \ref{f1}a) and rotate CCW, decreasing in amplitude over the next six days. By

October 30, the near surface velocities are almost due south with magnitudes of ~0.6 m s^{-1}, and remain relatively constant until the arrival of the front on early November 2.

Between October 24 (Fig. 1a) and October 29 (Fig. 1b), the warm water trough between the cold cusps lying just west of 140°W and 130°W appears to propagate southwest and then turns westward (Fig. 1c) before the southernmost point, just slightly west of the center of the trough, intersects the equator at 140°W on November 2 (Fig. 1e). The cold tongue appears to disperse beyond 140°W after the arrival of the front (Fig. 1d-f). A westward velocity component accompanied the front, and remained relatively constant through the rest of the IOP, while the meridional velocity component gradually transitioned from southward flow through zero to the north.

b. In-situ observations

TIW-generated meridional velocity variability on the Equator is strong at 140°W, penetrating below the thermocline, with periods ranging between 15 and 23 days (Lyman et al. 2007). The meridional velocity signal can be broken up into four phases as it transitions from north to south and back north again. During the IOP three of the four phases were observed: a northward phase, a north to south transition phase in which the meridional velocity went to zero, and a southward phase. Examples of vertical profiles of meridional and zonal velocities, potential

temperature and salinity during each of these three phases, as well as for the day the front passed through the EQUIX array, are plotted in Fig. 2 e-g. Meridional velocity variations during the phases of the TIW reach nearly 80 m, while perturbations to the velocity and density field during the translation of the front only affect the upper 40 meters (Fig. 2 e-g, solid black).

There was a strong diurnal cycle in SST (Fig. 2a), with a net warming of SST during the northward flowing phase at the beginning of the IOP that continued through October 29. A gradual cooling followed as the surface meridional current shifted to the south. The front is identified by the abrupt increase in SST on November 2. The SST increased by 0.45 °C within 7 s, which would correspond to a heating rate of 263 kW m^{-3} if imposed by processes other than advection; a rate far too high to be attributed to solar insolation, mixing or dissipation. After the passage of the front, the SST continued to increase, until it reached its maximum temperature of 26 °C on October 6, after which it gradually cooled through the rest of the observations. Sea surface salinity varied little before November 2, but decreased by 26 psu over 7 s with the passage of the front, after which the variability was greater and the surface water remained fresher (Fig. 2b). The overall change in density due to the temperature and salinity differences between the two surface water masses on either side of the front was -0.35 kg m^{-3}.

The meridional velocity was negative prior to the arrival of the front, with the upper 80 m flowing steadily southward at ~0.6 m s^{-1} (solid red line, Fig. 2f).

The zonal velocity was near zero at the surface and its vertical structure was dominated by the EUC, whose core resided at ~110 m and flowed east at ~1.4 m s^{-1} (Fig. 2e). The meridional component of vertical shear was restricted to the 20 m above the EUC core, below which meridional velocities diminished. Variability in zonal velocity above the EUC was small and possibly out of phase or perhaps even unrelated to meridional velocity, but its magnitude was abruptly and significantly altered with the passage of the front. The arrival of the front coincided with a westward increase of nearly 0.6 m s^{-1} at the surface, and a decrease of ~0.2 m s^{-1} in southward flow above the EUC. The zonal component of vertical shear above the EUC nearly tripled in response surface velocity adjustment that accompanied the front.

c. Detailed view of the front

Subsurface properties collected from the RV Wecoma over the 24 hour period surrounding the passage of the front are shown in Fig. 3. The time axis is shifted so that time zero refers to the time when the SST signature of the front was observed. Optical backscatter intensity (Fig. 3d) is a proxy for the relative concentration of particles within the water column. It is expected that the concentration would be relatively high within the cold tongue where upwelled nutrients are capable of sustaining a biologically active photic zone, as compared to the warm pool to the north where heavy rain fall below the ITCZ intensifies

stratification and hinders vertical mixing. The turbulent kinetic energy dissipation rate (ε, Fig. 3h) is indicative of the magnitude of turbulence and mixing.

The EUC is identifiable as the layer of strong, laminar (low ϵ), zonal flow below the sharp thermocline at $\sim$110 m. Over the 24 hour period surrounding the passage of the front the depth of the EUC oscillated slightly and gradually shoaled. The southward flow of the near surface waters above did not penetrate into EUC, and thus the EUC remained a strictly zonal flow during the period surrounding the front. Just above the EUC lies the Upper Core Layer (UCL); an anomalous, previously un-observed layer of strong dissipation isolated from the surface mixed layer (Moum et al. 2009; Inoue et al. 2012).

Above the UCL evenly spaced isopycnals outline three distinct bodies of water; all with comparable meridional velocity components of ~0.5 m s^{-1} (Fig. 3g). Over the twelve hours prior to the arrival of the front, the water column above 80 m can be divided into two distinct masses, each heading in different zonal directions. The upper 40 m was particle laden (Fig. 3d) and relatively cool and salty with temperatures ranging between 24.5°C and 24.75°C (Fig. 3b) and a salinity of ~34.32 psu (Fig. 3c); all expected characteristics of cold tongue water. It flowed south with the surrounding water, but exhibited small zonal velocity that fluctuated in sign (Fig. 3f).

Between the cold tongue water and 80 m, a quiescent layer with anomalously weak shear (Fig. 3h), stratification and dissipation flowed southward

with the surface water, but unlike the water above, flowed to the east at ~0.35 m s^{-1} (Fig. 3f). This quiescent layer was slightly cooler and denser than the water above, yet it was fresher and relatively devoid of suspended particles. Four hours before the arrival of the front the zonal velocity of the quiescent layer decreases before accelerating again below the surface frontal interface. While the vertical expanse of the quiescent layer is constricted after time zero, its temperature, salinity, particle concentration, and velocity remain constant, suggesting a lack of vertical mixing between it and the water masses above and below.

The surface water on the warm side of the front is outlined by the 1023.4 kg m^{-3} isopycnals, and extended to ~40 m within three hours of the front's passage (all panels Fig. 3). It was relatively warm and fresh and highly dissipative, with depth averaged ε exceeding 10^{-5} W kg^{-1} (Fig. 3h). Stratification increased below the warm front, as indicated by the vertical convergence of isopycnals, and properties of the water bounded by isopycnals were nearly identical across the front. A 20 m thick saline tongue with properties similar to those at the surface prior to the arrival of the front formed between the warm, fresh frontal mass and the quiescent layer (Fig. 3c) suggesting the possibility of subduction at the frontal interface. Vertical mixing of temperature, salinity and particle concentrations as well as zonal momentum occurred along the interface between the warm front water and the saline tongue. Oscillations in isopycnals which divide the two layers suggest the possibility of shear instabilities which can develop between two

tangent fluids with opposing trajectories. These instabilities are a mechanism that increases mixing.

4. Front Kinematics

a. Front propagation and orientation

The orientation of the front and its propagation speed can be found by comparing the time it takes the SST signal of the front to travel between components of the EQUIX array. If the front is linear in the horizontal plane and travels at a constant speed, then the time it takes the front to travel between two components of the array is equal to the distance between the components divided by the velocity at which the front is traveling.

SST time series during the translation of the front through the EQUIX site are plotted in Fig. 4a, with the arrival time of the SST signature of the front at each location labeled on the x-axis. In order to estimate the velocity of the front with these three measurements of SST, it is assumed that the velocity remains constant as it passes throughout the EQUIX region. With these assumptions, the velocity of the front can be calculated as the least squares error solution to the following equation (Hoecker-Martinez 2013):

Equation 1)

$$\Delta t_k + \Delta \tau_k = \frac{\Delta \vec{x}_k \cdot \vec{u}_f}{\vec{u}_f \cdot \vec{u}_f}$$

Here, the subscript *k* denotes location pairs, while Δt_k is the difference in arrival times between location pairs, $\Delta\tau_k$ is the error in time differences, $\Delta\vec{x}_k$ is the distance between location pairs and $\vec{u}_f$ is the velocity of the front.

The largest source of error comes from assuming that the front is linear, but a better assumption is not available. Another source of error comes from the low sampling rate of SST at the TAO mooring. The TAO mooring samples SST every 10 minutes making it the largest source of error. This error is decreased by assuming that the arrival time is constrained by the last time SST was below 25°C and the time the temperature increase is observed by the χ-pod at 18 m.

Calculating the propagation velocity twice, using each arrival time at the TAO mooring, we calculate that the front propagates at $c_f = |\vec{u}_f| = 0.56 \pm 0.01$ m s^{-1} to the heading 246.5° (WSW). The propagation and orientation are orthogonal, orienting the front 156.5° (WNW-ESE). The front's propagation speed c_f is listed in Table 1 along with other measured speeds observed during the IOP.

A new orthogonal coordinate system, based on the orientation of its propagation, is constructed by rotating compass coordinate unit vectors counter clockwise by 23.5° (upper left corner, Fig. 4b). The cross-front unit vector, $\hat{x}_c$ points parallel to the calculated front translation, while the along-front unit vector,

$\hat{y}_l$, points perpendicular to $\hat{x}_c$, parallel to (along) the front, and $\vec{u}_c$and $\vec{v}_l$ are their respective velocity components.

The local orientation of the front is compared with satellite images of SST from the Aqua MODIS daily composite SST for November 1, 2008 (Fig. 4b). The Aqua and Terra MODIS satellites pass over the equator twice each day. The AMODIS satellite passed over 0°N, 140°W and took measurement of SST at roughly 11:00 GMT on November 1, 2008. This image, therefore, represents the SST field roughly four hours before the passage of the front across the EQUIX array. The color for SST in Fig. 4b highlights the location and orientation of the leading edge of the front as the white region dividing cold-cusp water (blue) and the warm front (yellow). The calculated orientation of the front (black line, Fig. 4b) agrees well with satellite images of the front just before its arrival.

To investigate how the front's propagation compares kinematically to the observed near surface particle velocities measured by ADCPs, two periods on either side of the front are chosen to represent the background flow field into which the front propagated and the adjusted flow field that resulted in response to the front. These two periods would ideally be in steady state and hydrostatic balance for later analysis.

The pre-front steady state averaging period occurs after the subtle change in the quiescent layer flow four hours prior the front, and before the passage of the front. The post-front steady state averaging occurs after vertical structure of the

front has fully developed, roughly three hours after the front. The period of averaging is long enough to capture a mean flow, but not longer than the three hours over which the front's translation was assumed constant as it passed through the EQUIX site. The `before' and `after' time averages are defined as the 2 hour periods centered one hour directly preceding the arrival of the front, and four hours after the arrival of the front, respectively (Fig. 5).

The time-averaged near surface `before' and `after' velocity vectors are plotted with the calculated front speed, c_f, in Fig. 6. The `after' surface velocity is not parallel to the calculated propagation of the front, suggesting that the background flow field may be affected by processes other than forces normal to the front. To investigate further, the `before' and `after' near surface velocity vectors are decomposed into their respective across- and along-front components ($\vec{u}_{bfr}$, $\vec{u}_{aftr}$, Table 1), and compared in space (Fig. 6b-c). The near-surface cross-front flow increased by 0.32 m s^{-1}, while the along-front near surface flow decreased by 0.32 m s^{-1} ($\Delta\vec{u}$, Table 1).

b. Front reference frame

Time-depth plots similar to those in Fig. 3 but in a reference frame traveling 246.5° with the front are plotted in Fig. 7. The propagation speed of the front (c_f, Table 1) is subtracted from the cross-front velocity in order to help

visualize the system in a reference frame traveling with the front (Fig. 7f). Changes occurring around the front were confined to the near surface region and no obvious adjustments were made to or below the EUC. A few features are highlighted by this new perspective. The front was convergent, and its warm, fresh water, outlined by the 1023.7 kg m^{-3} isopycnal, exhibited a vertical circulation at its leading edge (Fig. 7f), with the cross-front velocity passing through zero just below 20 m, possibly due to the mixing of momentum with the underlying flow. The along-front velocity within the front is different than that of the surrounding water, but remains constant in time (Fig. 7e). It must be noted that Fig. 7 represents only changes in the cross-front direction and gives no information about changes that occurred along the front.

c. Two dimensional flow

Because observations are temporal, little is known about the along-front structure of the front. The flow can be approximated as two dimensional, and changes occurring in time interchangeable with changes occurring on the front's trajectory, if the along the front flow is in steady-state. To justify this assumption for the present case, changes occurring along the front are assessed, and continuity in the cross-front-vertical flow is demonstrated.

Comparisons between the velocity fields as observed at the EUQIX mooring and from the hull of the RV Wecoma are shown in Fig. 8a-b. This x-axis

is shifted for each data-set so that time zero refers to the arrival time of the front at each location. The frontal intersection with each component occurs at a different point along the linearly-assumed front. The along-front distance between the two observations is assumed to equal to the distance between intersection points and is just over 1.2 km between the RV Wecoma and the EQUIX mooring. The cross-front and along-front velocities are consistent between the two data sets (Fig. 8a, b), verifying that the along-front component of continuity is negligible along the observed section of the front, and suggesting that the changes in along-front velocity may be due to larger scale vortical flow within the traversing warm trough.

The flow is convergent across the front, and in order to conserve mass in a two dimensional cross-front-vertical flow, the horizontal convergence needs to be paired with a vertical divergence. If the denser water were subducted below the buoyant front, a process observed previously (Johnson 1996; Kennan and Flament 2000), continuity is assumed in the two dimensional flow. Subduction of cold tongue water below the front requires a negative vertical velocity, and the subducted water must conserve some physical properties. The vertical velocity, as shown by the upward facing 300-kHz ADCP on the EQUIX mooring shows an anomalous vertical velocity of -0.01 m s^{-1} at the leading edge of the front that extends to the base of the saline tongue described in section 3c (Fig. 3c), providing possible evidence for subduction of the streamline at the interface. It

should be noted that, while the amplitude of this signal is distinguishable from background noise, it is small in comparison with the rate of horizontal convergence at the front. Quite possibly the majority of the vertical velocity downwelling signal is small and lost to noise.

The presence of the cold saline tongue below the buoyant frontal mass in Fig. 3 is further evidence that subduction of denser water occurred at the front. Hourly-averaged potential temperature-salinity (θ-S) profiles show a distinct change in surface properties before and after the front (Fig. 9b). Post-front (warm colors, Fig. 9) surface properties are warmer and fresher than the pre-front (cool colors, Fig. 9) surface properties. Signatures of the pre-front surface water properties appear in the sub surface profiles of the warm side of the front, verifying that the cold, saline mass present below the front is indeed composed of the same water present at the surface before the front and supporting the hypothesis of subduction at the leading edge of the front.

d. Two-dimensional structure of the front

Mixing between the warm front and the subducted cold-cusp water is visible in the progressive smoothing of the θ-S profiles in time (red-yellow, Fig 9). This makes outlining the front difficult, as no information about the stratification of the warm trough prior to the subduction of the cold surface water

is available. I quantify the surface θ and S of the water masses on either side of the front, and by assuming θ and S are conserved physical properties, the depth to which the conserved properties of the surface water mass are subducted below the over-riding buoyant warm front. The θ-S signature of the surface water present before the arrival of the front can be used to define the temporal structure of the interface between the two masses on the warm side of the front, and the vertical shape of the over-riding flow.

To isolate the θ-S properties on either side of the front from diurnal heating effects and mixing across the front that occurred over time, surface properties of the `cold' and `warm' side of the front are defined by 30 min time-averages 7.5 min before and after the arrival of the front. These time-averages are produced from both the EQUIX mooring's surface SeaBird CTD and the Wecoma DAS, which are compared for accuracy and found to agree. The `cold' ambient surface properties are a temperature of 24.8°C, a salinity of 35.32 psu and a density of 1023.64 kg $m^{-3}$, and the `warm' front is defined by a temperature of 25.25°C, a salinity of 35.09 psu and a density of 1023.33 kg m^{-3}. These values will be used in the calculations performed in the next section, and their values are recorded in Table 2 for reference.

The boundary dividing the subducted water from the over-riding, buoyant front, and hence the vertical shape of the warm over-riding flow,$h(t)$, is defined as the polynomial fit to the upper boundary to which the θ-S signature of the

`cold' side of the front (Table 2) is identified in the water column after the front within a 95 \% confidence interval. The depth, $h(t)$, asymptotes to ~40 m within three hours of the front's arrival (white line, Fig. 7b-d, f-h). This value for h(t) encompasses both buoyant unmixed fluid flowing at the surface behind the front and a region of mixed concentrations of the surface fluids from both side of the front.

5. Comparison with a steady state gravity current

The dynamics of the two dimensional flow of the front resemble those of a turbulent gravity current. Gravity currents are predominantly horizontal flows generated by a density difference between two horizontally contiguous fluid masses. They can occur at ocean fronts where fresher and/or warmer water collides with and flows across denser water opposite the front (Simpson 1999). They have been observed on the ocean surface above the convergence point of the North Equatorial Front as `a line in the sea' of biological accumulation (Yoder et al. 1994; Johnson 1996), and below the surface where scattometers and echo-sounders outlined the cross-sections of the different water masses, and animated the flow of a buoyant current across denser ambient water below (Simpson 1999; Nash and Moum 2005) (Fig. 3d). Other common characteristic features of gravity currents, present here, are the sharp gradients in temperature and salinity at their leading edge, despite intense mixing which takes place within the advancing front (Fig. 3h), and the region below the front of mixed temperature, salinity and momentum, accompanied by oscillations in isopycnals, indicative of Kelvin-Helmholtz billows which often are observed in low viscosity flows (Simpson 1999)

a. Energy balance

The main force acting on such flows is the gravitational force, which is distributed unequally between the two adjacent fluids, and results in the descent of the denser fluid and the lateral spread of the buoyant fluid along the surface. Thus, potential energy (PE) is converted to kinetic energy (KE) at the front. In the case of perfect energy transfer, the upper limit of the speed of this current, c_0, is estimated by applying observed properties of the front to the following energy balance:

Equation (2)

$$PE = KE$$

$$\frac{1}{2} g' h_0 = \frac{1}{2} c_0^2$$

$$c_0 = \sqrt{g' h_0}$$

$$c_0 = 0.34 \text{ m s}^{-1}$$

Where $g' = g(\rho_a - \rho_c)/\rho_a$, is the reduced gravity, g is the gravitational constant, ρ_a = 1023.64 kg m^{-3} and ρ_c= 1023.33 kg m^{-3} are the densities of the ambient (`cold' side) and the current (`warm' side) established in section 3c (Table 2) and h_0 = 40 m is the asymptotic thickness of the front determined in section 3d.

b. Hydrostatic pressure gradient driven flow

Another way to interpret the dynamics along the frontal interface is to assume that the front is driven forward by the horizontal pressure gradient between the two bodies of water on either side of the front. Euler's equation for an incompressible, inviscid fluid at steading state in the across front direction is: Equation 3)

$$u_0(x)\frac{du_0(x)}{dx} = -\frac{1}{\rho_0}\frac{\partial P(x,z)}{\partial x}$$

Here, x is the cross-front horizontal coordinate, z is the vertical coordinate, u_0 is the speed of the pressure driven flow in the across front direction, and ρ_0 is a reference density set to $\rho_0 = \rho_a = 1023.64$ kg m^{-3}.

The pressure, $P(x,z)$, is obtained by the Chameleon profiler and is converted from a time dependent measurement to a cross-front dependent measurement through the following linear conversion:

$$x = ct$$

$$dx = cdt$$

Where c is an arbitrary constant that cancels between the left and right side of equation 3.

Integrating equation 3) horizontally across the front from a region infinitely far away, where the pressure is assumed to be zero, to an arbituary point, x', and then vertically through the depth of the warm current, h_0 = 40 m,

and solving for the root-mean-squared speed, $\bar{u}$, of the front at the leading edge of the current.

$$\frac{d}{dx}\left(\frac{1}{2}u_0^2(x)\right) = \frac{-1}{\rho_a}\frac{\partial}{\partial x}\big(P(x,z)\big)$$

$$\int_{-h_0}^{0}\int_{-\infty}^{x'}\frac{d}{dx}\left(\frac{1}{2}u_0^2(x)\right)\partial x\partial z = \int_{-h_0}^{0}\int_{-\infty}^{x'}\frac{-1}{\rho_a}\frac{\partial}{\partial x}\big(P(x,z)\big)\partial x\partial z$$

$$\frac{1}{h_0}\int_{-h_0}^{0}(u_0^2)dz = \bar{u}^2 = \frac{-2}{h_0\rho_a}\int_{-h_0}^{0}\big(P(z)\big)dz$$

$$\bar{u} = \sqrt{\frac{-2}{h_0\rho_a}\int_{-h_0}^{0}\big(P(z)\big)dz}$$

$$\bar{u} = 0.20\ m\ s^{-1}$$

The accuracy of this quantity is best evaluated by comparing the relative order of magnitude of the omitted terms in the momentum equations. These values will be included in a subsequent paper.

c. Lock-exchange gravity current models

An analytical model for two-dimensional, inviscid, gravity currents that combines the two balances calculated above is described by Benjamin (1968), and has proven quite useful due to its vigorous theoretical derivation, close comparisons to experimental results (Simpson 1999), and adaptability to a variety

of ambient conditions (Klemp et al. 1997; Ungarish 2006; White and Helfrich 2012; Xu 1992). In the model, a buoyant current of density ρ_c and thickness h propagates into a fluid filled channel of depth H and density $\rho_a > \rho_c$ at speed c_1 (Fig. 10). If viewing the system in a two dimensional reference frame moving with the front, the surrounding flow appears to move past a stationary object composed of the warm, buoyant mass on the warm side of the front. In this sense we can transform our perception of the changes occurring 'before' and 'after' the arrival of the front to the dynamics that occur 'upstream' and 'downstream' of the stationary object behind the front (Fig. 10). The 'upstream' flow, positioned at a sufficient distance from the front, is virtually unaffected by the presence of the object, while 'downstream' of the front, the background flow has undergone adjustments due to its interaction with the object. In the reference frame of the advancing front at the leading edge of the object, ambient parcels travel along streamlines between 'upstream' and 'downstream' locations, where the flow is assumed at steady state and in hydrostatic balance. The particles are accelerated to speed c_2, in order to conserve mass and momentum, as they travel past and below the `stationary' object.

The Benjamin (1968) model uses Bernoulli's equation to conserve momentum along streamlines and conservation of volume between the 'upstream' and 'downstream' flows. Bernoulli's Equation is frequently used in fluid dynamics to simplify the relationship between the pressure, velocity and height of

a parcel of ideal fluid in steady motion. Bernoulli's equation conserves momentum, by balancing inertial, potential and pressure terms within an incompressible fluid parcel as it travels along its streamline. In a reference frame moving with the advancing front, the pressure term can be thought of as the force necessary to hold the front at rest.

Benjamin (1968) provides a unique, energy conserving solution that occurs when the current fills exactly one half of the channel. At this state, $c_2 = \sqrt{g'h}$, and the flow below the horizontal interface of the 'stationary' buoyant current is super-critical with Froude number, $Fr = \frac{c_2}{\sqrt{g'(H-h)}} = \sqrt{2}$. The Froude number is a dimensionless parameter that relates inertial to gravitational forces. A Froude number greater than one is indicative of a super-critical flow. Super-critical flows are dominated by inertia, and can easily become unstable, as they form a hydraulic jump and dissipate into a thinner, stable, sub-critical flow. The dissipated energy of the unstable flow generates of internal waves and/or results in local turbulence.

An approximated bottom to the channel is placed at the sharp pycnocline above the EUC at ~100 m (Fig. 10b). The depth averaged transport, per unit width above this depth are 525 kg m^{-2} s^{-1} 'upstream' of the front, and 554 kg m-2 s-1 'downstream' of the front. Even with the liberal estimate of h_0, the current does not fill half the channel.

The Benjamin (1968) analysis also provides well-defined solutions to the decelerated speeds across the jump based on the fractional thickness of the current, $a = h/H$, and the reduced gravity, g'. Approximating H = 100 m, and $h = h_0 =$ 40 m:

Equation 4)

$$c_1 = \sqrt{g' h_0}\left[\frac{(2-a)(1-a)}{(1+a)}\right]^{\frac{1}{2}} = 0.28\ m\ s^{-1}$$

Equation 5)

$$c_2 = \frac{c_1}{(1-a)} = 0.47\ m\ s^{-1}$$

This flow is sub-critical with a Froude number of 0.20.

The approximation of H = 100 m is not well supported; however, an increase (decrease) of 10% to the system's depth results in an increase (decrease) of 0.02 m s^{-1} in c_1, and a decrease (increase) of 0.01 m s^{-1} in c_2.

Assumptions made by the original Benjamin (1968) model are that the fluids are inviscid and homogenous, and that the current propagates into an ambient with zero background flow. The results from the Benjamin (1968) model agree well with the calculation of $\bar{u}$, but neither takes into account the effects of the strong cross-front vertical shear into which the buoyant current is propagating. Headwinds and opposing shear decrease the thickness of a gravity current and its propagation speed (Xu 1992; Simpson 1999).

The observed background flow ('upstream', Fig. 5a) has considerable vertical shear, which ranges from -0.01 s^{-1} above the quiescent layer to -0.03 s^{-1} above the EUC. A schematic for an adaptation to the Benjamin (1968) model which includes a linearly sheared ambient (Xu 1992) is shown in Fig. 11a. Parcels conserve mass and momentum along streamlines between 'upstream' and 'downstream' locations, as in the Benjamin (1968) model, but solutions for the propagation speed of the surface signal $c_1 = U_{in}(z = 0)$, the thickness of the current, h, and an outflow speed relative to the current of $c_2 = U_{out}(z = h)$, are quantified for flows which conserve both energy and vorticity as functions of the linear ambient vertical shear, $\alpha = \frac{\partial}{\partial z} U_{in}(z)$.

The idealized energy and vorticity conserving solutions are over constrained and depend on the vertical ambient shear, the depth of the channel, and the reduced gravity between the two adjacent fluids (Fig. 11b). The current thickness is not an independent parameter as it was in the three preceding calculations. The dimensionalized solutions in a channel of depth H = 100 m with a vertical shear of α = -0.01 s^{-1} (red, Fig. 11b) results from a buoyant current of thickness h = 16 m, that propagates at c_1 = 0.12 m s^{-1}. Increases (decreases) of 10% to the depth of the channel do not affect c_1, but increase (decrease) c_2 by 0.01 m s^{-1} and increase (decrease) the expected depth of the current by 1 m.

6. Discussion

To a first order approximation $\bar{u}$ provides the best approximation to the hydrostatic-pressure-gradient driven flow because it is based on measured properties. Comparisons between it and the Benjamin (1968) and Xu (1992) models provides some insight into the effects that the opposing shear of the ambient may have had on the buoyant current. The analytical models are based on two homogenous, inviscid fluids, and neither accounts for the region of mixed fluid accumulated below the buoyant current. Assuming that the entire 40 m thick current was unmixed and composed of only the buoyant fluid results in an overestimation of the pressure-gradient force in the Benjamin (1968) model; while assuming that the region below the 16 m buoyant current was composed of un-mixed dense ambient water results in an underestimation of the pressure-gradient force in the Xu (1992) model.

The idealized solution provided by the (Xu 1992) model reflects a current that is significantly thinner than observed and which propagates slower than the other estimates (Table 3). While the Benjamin (1968) model provides solutions to the non-energy conserving flow if provided with a fractional current thickness, $a = h/H$, solutions to the Xu (1992) model require experimentally derived inputs of both dissipation and vorticity generation. Non-idealized solutions result in thinner currents than those that conserve energy and vorticity (Fig. 11), which can

be either in a sub- or super-critical state. A case may still be argued that the front's thickness, h_0, was an upper-bound to the current's thickness, h, and included a region of mixed fluid. In this case, the mixed region encompasses at least h/h_0 = 40% of the front's vertical extent.

Assuming that $\bar{u}$ accounts for the internally-driven propagation speed of a gravity current embedded within the mesoscale west-ward propagating TIW, it accounts for the sudden change in near surface velocity that corresponded with the passage of the front. This suggests that the observed, near-surface zonal velocity before the arrival of the front was due to the westward propagation of the TIW. The calculation of the TIW propagation computed in section 3a is not precise and a better approximation using the long-term velocity data from the TAO mooring will be computer in a successive paper. For now, a westward propagation speed of 0.5 ± 0.1 m s^{-1} accounts for the observed, near-surface zonal velocity before the arrival of the front.

Observations of the behavior of the front suggest that it is locally independent of the westward propagating perturbations by the TIW which alter the meridional velocity within the upper 80 m. The anomalous 40 m buoyant mass shares more features with those of a gravity current. These features include the propagation of a turbulent buoyant fluid into a denser ambient which forces the denser fluid to be subducted below. The gravity current hypothesis is further

supported by the existence of the SST signature 1.5 hr later despite vigorous mixing between the subducted fluid with the over-riding buoyant current.

Satellite images of SST during the IOP suggest that the front was advected southward along with a TIW warm trough (Fig. 1). As it approached the equator, it appears to have turned west. The change in along-front velocity across the front suggests that the warm trough was rotating. Possibly this rotation was an effect of the anti-cyclonic circulation within the mesoscale TIW warm trough. As southward advection drove the mesoscale feature near the equator, it is possible that a non-linear, super-critical gravity current flow was able to escape across the front in the absence of corriolis.

7. Conclusion

The sharp jump in SST that was observed on Nov 2, 2008 was attributed to the southward advection of the NEF oriented along the SW corner of a TIW generated warm water trough. The front propagated SSW at 0.56 m s^{-1}, redirecting surface flow, and over-riding equatorial cold tongue water present at the surface prior to its passage. Observations suggest that the over-riding flow behind the front was driven by a hydrostatic-pressure gradient force and flowed as a gravity current embedded within the westward propagating TIW. Internal driving forces of a gravity current account for the increase in across-front velocity that accompanied the front, but were not large enough to account for the total observed propagation speed of the front, indicating the importance of both hydrostatic-pressure gradient forces and the westward propagation of the TIW.

BIBLIOGRAPHY

Benjamin, T. B., 1968: Gravity currents and related phenomena. **31 (2)**, 209248, URL http://journals.cambridge.org/production/action/cjoGetFulltext?fulltextid=366020.

Chelton, D. B., F. J. Wentz, C. L. Gentemann, R. A. de Szoeke, and M. G. Schlax, 2000: Satellite microwave set observations of transequatorial tropical instability waves. *Geophysical Research Letters*, **27 (9)**, 1239-1242.

Cox, M. D., 1980: Generation and propagation of 30-day waves in a numerical model of the pacific. *Journal of Physical Oceanography*, **10 (8)** 1168-1186.

de Szoeke, S. P., S.-P. Xie, T. Miyama, K. J. Richards, and R. J. O. Small, 2007: What maintains the SST front north of the eastern pacific equatorial cold tongue?. **20 (11)**, 2500-2514, doi:10.1175/JCLI4173.1, URL http://journals.ametsoc.org/doi/abs/101175/JCLI4173.1.

Flament, P. J., S. C. Kennan, R. A. Knox, P. P. Niiler, and R. L. Bernstein, 1996: The three-dimensional structure of an upper ocean vortex in the tropical pacific ocean. *Nature*, **383 (6601)**, 610–613.

Gregg, M., H. Peters, J. Wesson, N. Oakey, and T. Shay, 1985: Intensive measurements of turbulence and shear in the equatorial undercurrent. *Nature*, **318 (6042)**, 140–144.

Hoecker-Martinez, M., 2013: Clocking a front. URL http://wart.coas.oregonstate.edu/Documents/localwiki/doku.php?id=blog:where_did_that_come_from.

Holmes, R. M., L. N. Thomas, L. Thompson, and D. Darr, 2013: Potential vorticity dynamics of tropical instability vortices. wiley.com/10.1029/2011JC007767.

Inoue, R., R.-C. Lien, and J. N. Moum, 2012: Modulation of equatorial turbulence by a tropical instability wave. **117 (c10)**, doi:10.1029/2011JC007767, URL http://doi.wiley.com/10.1029/2011JC007767.

Johnson, E. S., 1996: A convergent instability wave front in the central tropical pacific. **43 (4)**, 753778, URL http://www.sciencedirect.com/science/article/pii/ 560 0967064596000343.

Kennan, S. C. and P. J. Flament, 2000: Observations of a tropical instability vortex*. **30 (9)**, 22772301, URL http://journals.ametsoc.org/doi/abs/10.1175/1520-0485(2000)030%3C2277:OOATIV%3E2.0.CO;2.

Klemp, J. B., R. Rotunno, and W. C. Skamarock, 1997: On the propagation of internal bores. **331**, 81106, URL http://journals.cambridge.org/production/action/cjoGetFulltext?fulltextid=5596752.

Lee, T., G. Lagerloef, M. M. Gierach, H.-Y. Kao, S. Yueh, and K. Dohan, 2012: Aquarius reveals salinity structure of tropical instability waves. **39 (12)**, doi:10.1029/2012GL052232, URL http://doi.wiley.com/10.1029/2012GL052232.

Legeckis, R., 1977: Long waves in the eastern equatorial pacific ocean: A view from a geostationary satellite. *Science*, **197 (4309)**, 1179–1181.

Lien, R.-C., E. A. D'Asaro, and C. E. Menkes, 2008: Modulation of equatorial turbulence by tropical instability waves. **35 (24)**, doi:10.1029/2008GL035860, URL http://doi.wiley.com/10.1029/2008GL035860.

Moum, J. N., R.-C. Lien, A. Perlin, J. D. Nash, M. C. Gregg, and P. J. Wiles, 2009: Sea surface cooling at the equator by subsurface mixing in tropical instability waves. **2 (11)**, 761765, doi:10.1038/ngeo657, URL http://www.nature.com/doifinder/10.1038/ngeo657.

Nash, J. D. and J. N. Moum, 2005: River plumes as a source of large-amplitude internal waves in the coastal ocean. **437 (7057)**, 400403, doi:10.1038/nature03936, URL http: //www.nature.com/doifinder/10.1038 /nature03936.

Philander, S., 1976: Instabilities of zonal equatorial currents. *Journal of Geophysical Research*, **81 (21)**, 3725–3735.

Philander, S., 1978: Instabilities of zonal equatorial currents, 2. *Journal of Geophysical Research*, **83 (C7)**, 3679–3682.

Qiao, L. and R. H. Weisberg, 1995: Tropical instability wave kinematics: Observations from the tropical instability wave experiment. *Journal of Geophysical Research: Oceans (1978–2012)*, **100 (C5)**, 8677–8693.

Qiao, L. and R. H. Weisberg, 1998: Tropical instability wave energetics: observations from the tropical instability wave experiment. *Journal of Physical Oceanography*, **28 (2)**, 345-360.

Simpson, J. E., 1999: *Gravity currents: In the environment and the laboratory*. Cambridge University Press.

Ungarish, M., 2006: On gravity currents in a linearly stratified ambient: a generalization of benjamin's steady-state propagation results. **548 (-1)**, 49, doi: 10.1017/S0022112005007421, URL http://www.journals.cambridge.o rg/abstract_ 609 S0022112005007421.

White, B. L. and K. R. Helfrich, 2012: A general description of a gravity current front propagating in a two-layer stratified fluid. 711, 545–575, doi:10.1017/jfm.2012.409, URL http://www.journals.cambridge.org/abstract_S0022112012004090.

Xu, Q., 1992: Density currents in shear flows-a two-fluid model. *Journal of atmospheric sciences*, **49 (6)**, 511–524.

Yoder, J. A., S. G. Ackleson, R. T. Barber, P. Flament, and W. M. Balch, 1994: A line in the sea. *Nature*, **371 (6499)**, 689–692.

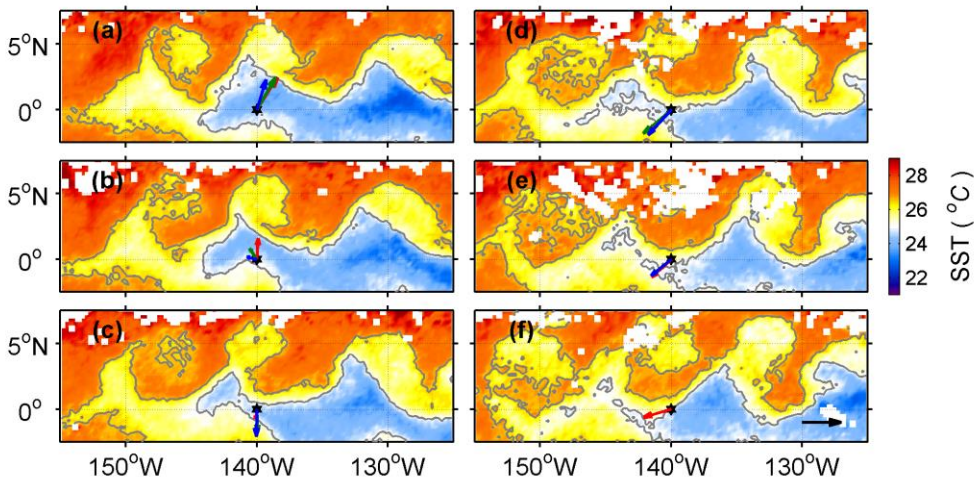

FIG. 1. TRMM TMI 3-day composite averaged SST of the active TIW during the Intensive Observation Period (IOP) of the EQUIX experiment centered on (a) October 25, (b) October 28, (c) the October 31, (d) November 3, (e) November 6 and (f) November 10. Black stars at 0°N, 140°W indicate the EQUIX site. Vectors represent daily averaged near surface (z = 10 m) ADCP velocity measurements for the first (red), second (green) and third (blue) day of each composite period. For scaling, a 1 m s^{-1} velocity vector is shown in black on the bottom right corner of (f). Gray contours show the 25°C and 26.5°C isotherms. The 25°C contour identifies the front observed by the EQUIX array.

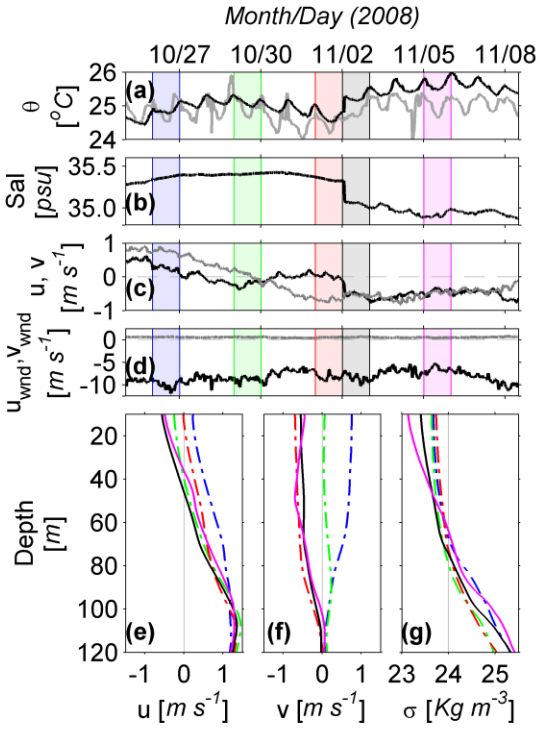

FIG. 2. Time series during the 16-day Intensive Observation Period (IOP) of (a) SST (black) and 1 hour low-pass filtered air temperature (gray), (b) surface salinity, (c) 1 hour low-pass filtered zonal (black) and meridional (gray) near surface (10 meter depth) velocities, and (d) 1 hour low-pass filtered zonal (black) and meridional (gray) wind velocities). (Note: Wind velocities are in oceanographic convention, i.e. the direction the wind is heading toward.) Daily averaged profiles of (d) Zonal velocity, (e) Meridional velocity, and (f) potential density, for 26 October (blue, dash-dot), 29 October (green, dash-dot), 1 November (red, dash-dot) 2 November (black), and 5 November (magenta). Averaging periods are shaded in a-d.

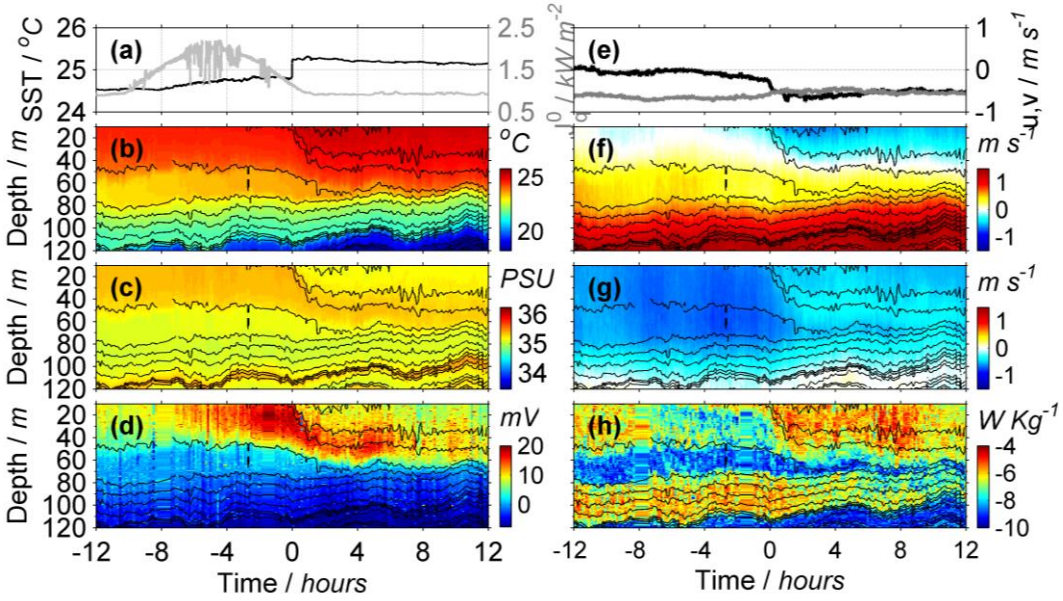

FIG. 3. Measurements from the RV Wecoma during the 24-hour period surrounding the arrival of the front. Time zero refers to the time when the 25°C SST contour passed the Wecoma. Time series of (a) SST (black) and surface heat flux (gray), and (e) zonal (black) and meridional (gray) near surface velocities. (b) Potential Temperature, (c) salinity, (d) optical backscatter, (f) zonal velocity, (g) meridional velocity, and (h) turbulent kinetic energy dissipation rate, ε. Isopycnal contours beginning at 1023.25 kg m-3 and increasing by 0.15 kg m-3 increments are in black.

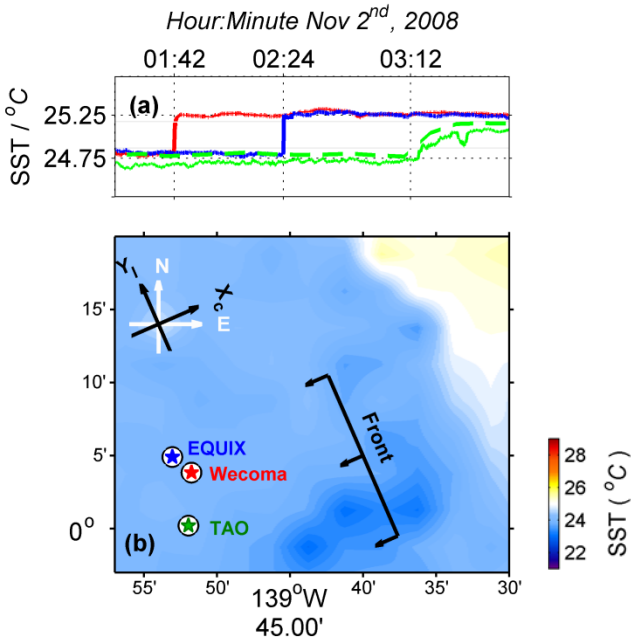

FIG. 4. (a) High resolution SST time-series from Wecoma DAS (red), EUQIX surface Seabird SBE37 pumped CTD sensor (blue), Tropical Ocean Global Atmosphere Tropical Atmosphere Ocean (TOGA TAO) mooring at 0°N, 140°W (dashed green), and a microstructure X-pod attached to the TAO mooring at ~18 m depth (solid green). Sampling rates were 2 s, 7 s, hourly averaged and 0.1 s, respectively. (b) Aqua Spacecraft Moderate Resolution Imaging Spectra-radiometer (AMODIS) Level-3 4km NSST from November 1, 2008. Colored stars indicate the locations of each array component at the time of the front passage. The calculated front orientation is labeled in black with orthogonal vectors indicating the magnitude and direction of propagation. Unit vectors for a front-space coordinate system are plotted in black in the upper left corner.

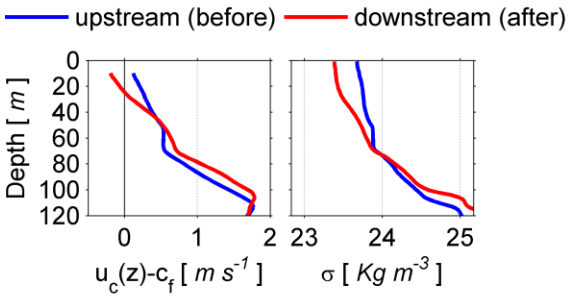

FIG. 5. Time averaged profiles of (a) cross-front velocity minus the front propagation speed, $\boldsymbol{c_f}$, and (b) potential density from the 'before' ('upstream', blue) and 'after' ('downstream', red) averaging periods. Time averaging periods are explained in section 4a. The 'before' and 'after' periods are the 2 hours directly proceeding the front and 3 to 5 hours after the front.

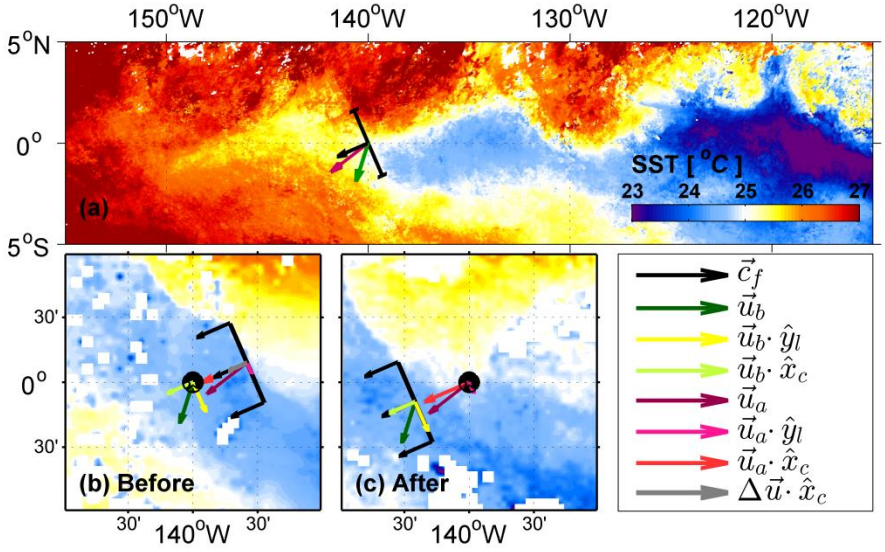

FIG. 6. (a) Aqua MODIS Level-3 8-day SST composite for October 31 through November 7. (b) Aqua MODIS Level-3 4km NSST from November 1 and (c) Terra MODIS Level-3 4km SST from November 2. The Aqua satellite passed over the equator and 140°W at approximately 11:00 GMT on November 1, 2008, and the Terra satellite passed over the same location at approximately 19:30 GMT on November 2, 2008. Black arrows in panels (a)-(c) represent the calculated front propagation, while the accompanying orthogonal black line defines its orientation. The green (purple) vector indicates the time averaged near surface velocity over the 'before' ('after') period, while its corresponding along-front component is plotted in yellow (magenta) and cross-front component in bright green (red). The difference in the across-front velocity between the two time averaged periods is shown in gray.

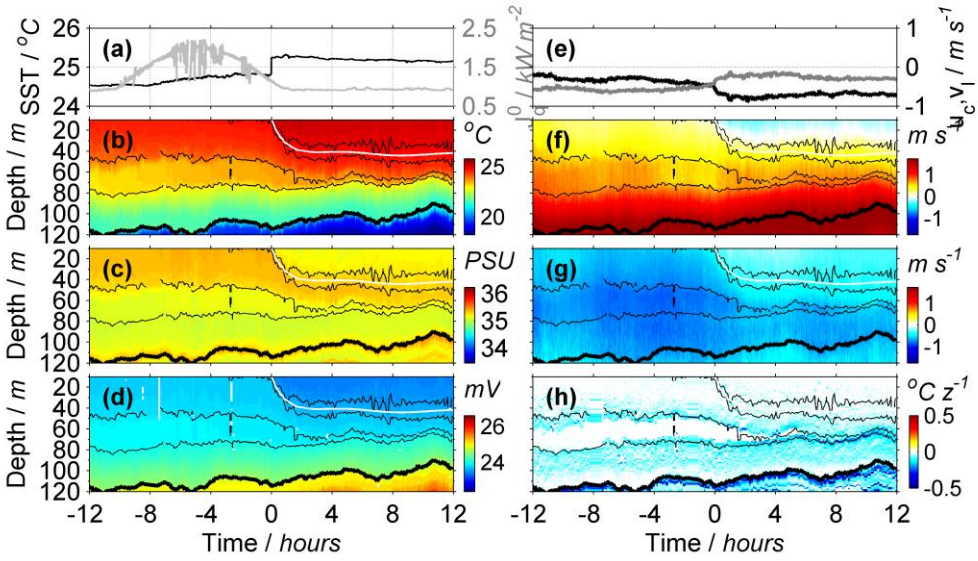

FIG. 7. Measurements oriented with frontal progression from the RV Wecoma during the 24 hour period surrounding the arrival of the front. Time zero refers to the time when the SST signature of the front passed the ship. Time series of (a) SST (black) and surface heat flux (gray), and (e) along-front (black) and cross-front (gray) near surface velocities. The frontal coordinate system is plotted in Fig. 4b. (b) Potential Temperature, (c) salinity, (d) potential density, (f) cross-front velocity minus the front's propagation speed, (g) along-front velocity, and (h) vertical temperature gradient, $\boldsymbol{T_z}$. The thin black lines represent isopycnal contours ranging between 1023.55 kg m^{-3} and 1024.00 kg m^{-3} in increments of 0.15 kg m^{-3}. The thick black line outlines the 1024.75 kg m^{-3} isopycnal, and the thin white line is the lower boundary of the buoyant surface current, $\boldsymbol{h(t)}$, described in section 4d.

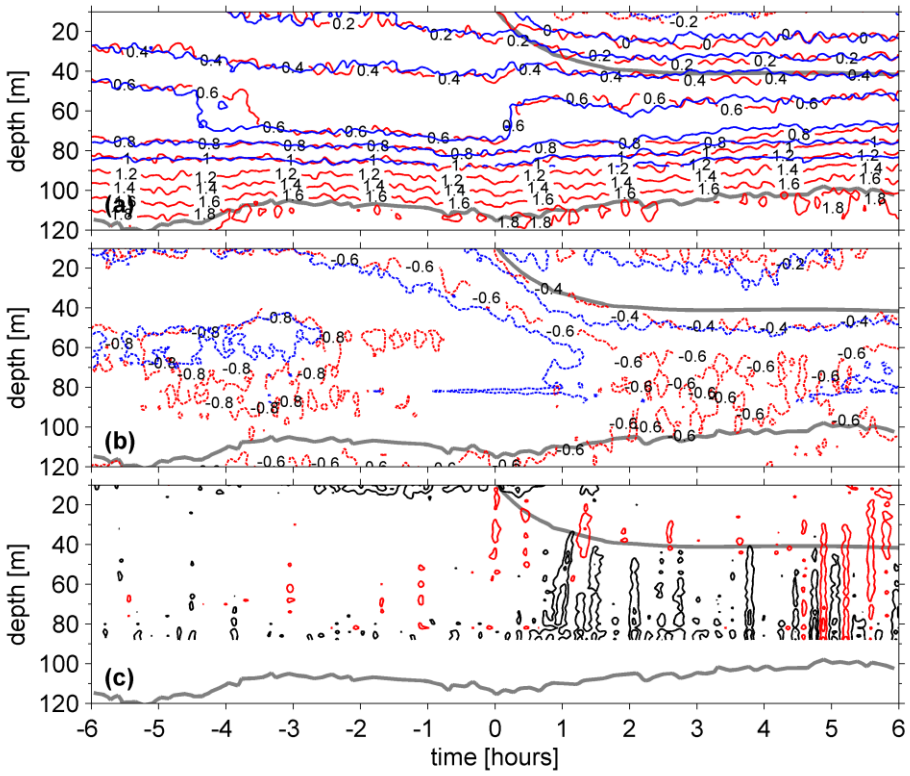

FIG. 8. 10-minute averaged contours of (a) cross-front velocity minus the front propagation speed, $\boldsymbol{c_f}$, and (b) along-front velocity obtained from the RV Wecoma 300-kHz ADCP (red) and the EQUIX 300-kHz ADCP (blue) at 0.2 m s^{-1} intervals. Solid (dashed) lines indicate positive (negative) velocities. (c) 10-minute averaged contours of vertical velocity from the EQUIX 300 kHz ADCP at 1 cm s^{-1} intervals (omitting the zero velocity contour for clarity), with positive (negative) contours in black (red). Time zero in each plot refers to the time when the SST signature of the front crosses each respective array component. Gray contours indicate the estimated vertical shape of the buoyant overriding fluid on the warm side of the front, $\boldsymbol{h(t)}$, and the 1024.75 Kg m^{-3} isopycnal.

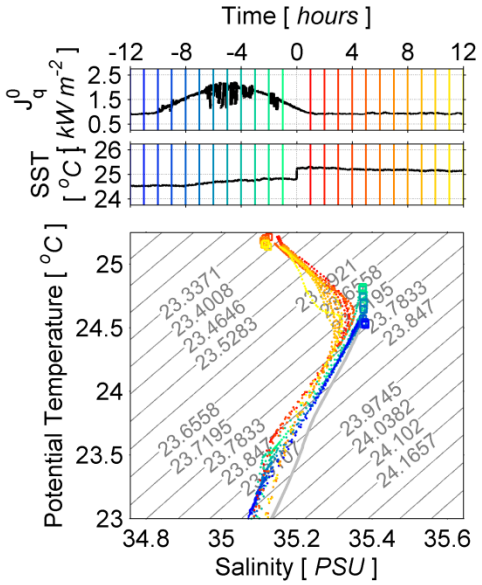

FIG. 9. Time-series of SST (a) and surface heat flux, $\boldsymbol{J_q^0}$, (b). Colored vertical lines indicate central points of time averaging used in corresponding color profiles in lower panel. (c) Color coded hourly averaged Temperature-Salinity (θ-S) profiles within the 24 hour period surrounding the passage of the front past the RV Wecoma. Colored squares represent hourly averaged surface properties obtained from the RV Wecoma shipboard underway data acquisition system (DAS). Colored dots mark potential temperature and salinity every meter between 10 and 80 meters depth as measured by the Chameleon profiler. The thick gray curve defining the daily average of temperature and salinity on November 1 is added for reference. Thin gray lines indicate surfaces of constant density in θ-S space.

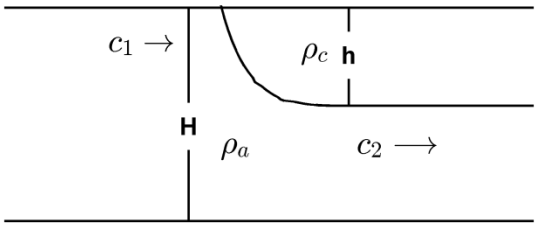

FIG. 10. Schematic of the Benjamin (1968) analytical lock-exchange gravity current model in the reference frame propagating at $\boldsymbol{c_1}$ with the front of a gravity current of thickness $\boldsymbol{h}$ and density $\boldsymbol{\rho_c}$ across a horizontal channel of depth $\boldsymbol{H}$ and density $\boldsymbol{\rho_a > \rho_c}$, above an outflow current of $\boldsymbol{c_2}$.

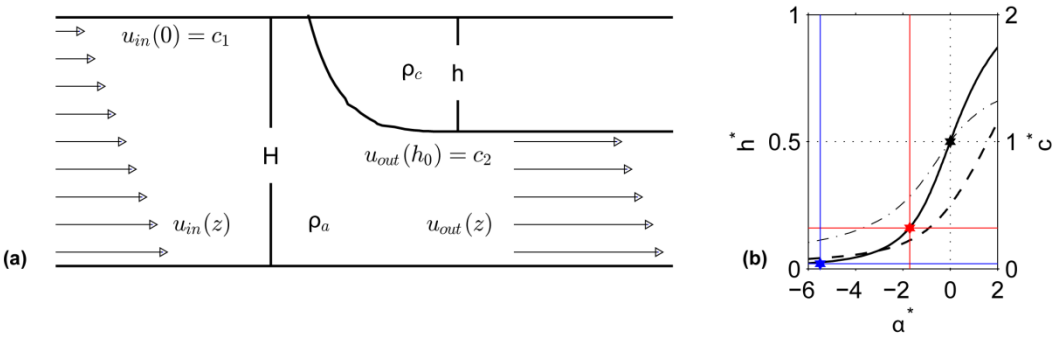

FIG. 1. (a) Schematic of the Xu (1992) analytical lock-exchange gravity current model in the reference frame propagating at $\boldsymbol{c_1}$ with the front of a gravity current of thickness $\boldsymbol{h}$ and density $\boldsymbol{\rho_c}$ across a linearly sheared horizontal channel of depth $\boldsymbol{H}$ and density $\boldsymbol{\rho_a > \rho_c}$, above an outflow current of $\boldsymbol{c_2}$. The vorticity conserving background shear is $\boldsymbol{U_{in}(z)}$ 'upstream' of the current and $\boldsymbol{U_{out}(z)}$ 'downstream' and below. (b) Scaled depth, $\boldsymbol{h^* = h/H}$ (solid black), and propagation speeds, $\boldsymbol{c_1^* = c_1/\sqrt{g'H}}$ (dashed, black) and $\boldsymbol{c_2^* = c_2/\sqrt{g'H}}$ (dot-dashed, black), of the energy and vorticity conserving flow as functions of scaled ambient shear, $\boldsymbol{\alpha^* = \alpha H/\sqrt{g'H}}$. Energy and vorticly conserving solutions for an ambient shear, $\boldsymbol{\alpha = \frac{d}{dz}U_{in}(z)}$, of 0.00 s^{-1} (black dotted), -0.01 s^{-1} (red) and -0.03 s^{-1} (blue) are marked for reference to the observed flow.

	u_c	v_l
U_{TIW}	$-0.37\,m\,s^{-1}$	$0.16\,m\,s^{-1}$
$\vec{c}_f$	$-0.56\,m\,s^{-1}$	$0.00\,m\,s^{-1}$
$\vec{u}_{bfr}$	$-0.44\,m\,s^{-1}$	$-0.51\,m\,s^{-1}$
$\vec{u}_{aft}$	$-0.76\,m\,s^{-1}$	$-0.19\,m\,s^{-1}$
$\Delta\vec{u}$	$-0.12\,m\,s^{-1}$	$0.51\,m\,s^{-1}$

TABLE 2. Observed velocities in the frontal coordinate system defined in section 4a for the westward propagation speed, $\boldsymbol{U_{TIW}}$, of the TIW defined in section 3a, the propagation speed of the front, $\boldsymbol{c_f}$, determined in section 4a, and the time averaged, near-surface particle velocities from 'before' and 'after' the front described at the end of section 4a.

	θ	Sal	σ
$coldside$	$24.8\,°C$	$35.32\,psu$	$23.64\,kg\,m^{-3}$
$warmside$	$25.25\,°C$	$35.09\,psu$	$23.33\,kg\,m^{-3}$

TABLE 3. Surface water properties from the ‘cold’ (ambient) and ‘warm’ (current) defined in section 4d.

	$\lvert u_c \rvert$
c_0	$0.34\,m\,s^{-1}$
$c_{1,Be}$	$0.28\,m\,s^{-1}$
$c_{1,Xu}$	$0.12\,m\,s^{-1}$

TABLE 4. Estimated frontal propagation speeds from the balances and models presented in section 5. Subscripts Be and Xu distinguish the propagation speed $\boldsymbol{c_1}$ derived by the Benjamin (1968) and Xu (1992) models.